

## Progression of failure in fiber-reinforced materials

R. Han, M. S. Ingber\*, H. L. Schreyer

*Department of Mechanical Engineering, University of New Mexico,  
Albuquerque, NM 87131, U.S.A.*

### SUMMARY

Decohesion is an important failure mode associated with fiber-reinforced composite materials. Analysis of failure progression at the fiber-matrix interfaces in fiber-reinforced composite materials is considered using a softening decohesion model consistent with thermodynamic concepts. In this model, the initiation of failure is given directly by a failure criterion. Damage is interpreted by the development of a discontinuity of displacement. The formulation describing the potential development of damage is governed by a discrete decohesive constitutive equation. Numerical simulations are performed using the direct boundary element method. Incremental decohesion simulations illustrate the progressive evolution of debonding zones and the propagation of cracks along the interfaces. The effect of decohesion on the macroscopic response of composite materials is also investigated. Copyright © 2005 John Wiley & Sons, Ltd.

KEY WORDS: composite materials; decohesion model; incremental debonding, boundary element method

### 1. INTRODUCTION

High-performance composite materials comprised of a dispersed phase (inclusions) suspended in a matrix material combine the advantage of high structural strength with complementary properties such as light weight, high or low thermal and electrical conductivity, and prescribed coefficient of thermal expansion. The versatility and low unit cost of these materials make them well-suited for lightweight structural components, shock and thermal insulators, encapsulants for electronic components, and functionally graded materials (FGMs).

The performance of these materials is highly dependent on the interfacial characteristics between the inclusions and the matrix material. There is a large body of literature on the effective thermomechanical properties for this class of composite materials under the assumption of perfect bonding, i.e., no jump in displacement and no contact resistance. Models for these effective properties have been based on (i) semiempirical techniques [1, 14, 20], (ii) variational approaches using extremum principles [11, 8, 2], (iii) self-consistent schemes [16,

---

\*Correspondence to: Department of Mechanical Engineering, University of New Mexico, Albuquerque, NM 87131, U.S.A.

6, 19], and (iv) numerical experiments [12, 7, 13]. Several excellent review articles and books have been written on this subject [9, 25, 18].

There have been some investigations of the effective properties of composite materials with imperfect interfaces such as contact resistance for the thermal problem [5, 15] and debonding for the elasticity problem [10, 23, 4]. However, these studies have assumed somewhat idealized interfacial conditions. For example, Chati and Mitra [4] and Sangani and Mo [23] assume that segments of the interface are either fully adhered or completely decohered (traction free). That is, these studies have not accounted for the progression of failure along the interface.

Needleman [17] proposed a debonding mechanism based on interfacial ductility by allowing two initially coincident points, one on the inclusion and one on the matrix material, to move apart from each other when under load. The interfacial traction was then a function of the jump in displacement. Needleman adopted a function that initially produced increasing traction as the interfacial separation increased, went through a maximum, and subsequently decayed to zero as the separation increased further.

Salvadori [22] proposed a similar approach in terms of a smoothing locking constitutive law, which provided normal and shear tractions as a function of interface opening and sliding, i.e., the tangential and normal jump in displacement. Tractions and displacement discontinuities were related through an exponential function which essentially spanned the region from perfectly bonded to a stress free surface at the interface. The numerical implementation for problems with traction-free cracks and rigidly bonded perfect interfaces was performed using a symmetric Galerkin boundary element method (BEM).

The discrete constitutive equations of Needleman [17] and Salvadori [22] can be considered special cases of a broad category that are analogous to both elastic-plastic and damage constitutive equations for a continuum. Schreyer *et al.* [24] provides a fairly general formulation of a discrete constitutive equation under the assumption that the displacement discontinuity contains no elastic component. Both associated and non-associated forms were given to illustrate the generality of the approach. A plastically softening decohesion formulation can be used in conjunction with any continuum constitutive equation to provide a method for modeling failure either interior to the matrix or along an interface.

In the current research, a particular form of the model with an associated flow rule of Schreyer *et al.* [24] is extended to include the situation where the normal component of the traction vector can be negative. The resulting formulation is combined with the boundary element method (BEM) to investigate decohesion of fiber-reinforced composite materials. The boundary element formulation for the multiply-connected zoned-homogenous domain is presented in Section 2. The decohesion model along with its numerical implementation is presented in Section 3. Several example problems are considered in Section 4 for both brittle and ductile failure. Finally, conclusions are presented in Section 5.

## 2. BOUNDARY ELEMENT FORMULATION

In the current study, the computational domain is considered to be comprised of a matrix material with embedded aligned long fibers allowing the governing equations to be reduced to the plane strain equations. These equations can be recast in integral form by considering the associated weak form, applying the Green-Gauss divergence theorem twice, and choosing the fundamental solutions for displacement and traction as the weighting functions [3]. The

appropriate expressions for the two-dimensional fundamental displacements and associated tractions for plane strain are given by

$$u_{ij}^*(\mathbf{x}, \mathbf{y}) = \frac{-1}{8\pi(1-\nu)G} \{(3-4\nu) \log r \delta_{ij} - r_{,i} r_{,j}\} \quad (1)$$

$$t_{ij}^*(\mathbf{x}, \mathbf{y}) = \frac{-1}{4\pi(1-\nu)r} \left\{ [(1-2\nu)\delta_{ij} + 2r_{,i} r_{,j}] \frac{\partial r}{\partial n} - (1-2\nu)(r_{,i} n_j - r_{,j} n_i) \right\} \quad (2)$$

where  $r$  is the distance between  $\mathbf{x}$  and  $\mathbf{y}$ ,  $n_i$  is the component of the unit outward normal vector to the boundary,  $G$  is the shear modulus,  $\nu$  is the Poisson ratio and the comma denotes differentiation with respect to the appropriate Cartesian coordinate. The resulting boundary integral equation (BIE) for the displacement components is given by

$$c_{ij}(\mathbf{x}) u_j(\mathbf{x}) = \int_{\Gamma} u_{ij}^*(\mathbf{x}, \mathbf{y}) t_j(\mathbf{y}) d\Gamma(\mathbf{y}) - \int_{\Gamma} t_{ij}^*(\mathbf{x}, \mathbf{y}) u_j(\mathbf{y}) d\Gamma(\mathbf{y}) \quad (3)$$

where  $\Gamma$  is the boundary of the domain  $\Omega$ ,  $u_j$  and  $t_j$  are the components of displacement and traction on the surface  $\Gamma$ , respectively. The coefficient  $c_{ij}$  can be determined from the equation

$$c_{ij}(\mathbf{x}) = - \int_{\Gamma} t_{ij}^*(\mathbf{x}, \mathbf{y}) d\Gamma(\mathbf{y}) \quad (4)$$

The boundary integral equation is discretized by subdividing the boundary  $\Gamma$  into boundary elements. The boundary element used in this research is the three-node, isoparametric quadratic element. Hence, within each element  $u_i(\mathbf{y})$  and  $t_i(\mathbf{y})$  are approximated as

$$u_i^e(\mathbf{y}) | \Gamma_e \approx \sum_{k=1}^3 u_{ik}^e \Psi_k(\mathbf{y}) \quad (5)$$

$$t_i^e(\mathbf{y}) | \Gamma_e \approx \sum_{k=1}^3 t_{ik}^e \Psi_k(\mathbf{y}) \quad (6)$$

where  $u_{ik}^e$  and  $t_{ik}^e$  represent the values of  $u_i$  and  $t_i$ , respectively, at the  $k^{th}$  node within the  $e^{th}$  element, and  $\Psi_k$  represents the quadratic shape functions.

Using the above approximations, the discretized form of the boundary integral equation is given by

$$c_{ij}(\mathbf{x}) u_j(\mathbf{x}) = \sum_{e=1}^{ne} \sum_{k=1}^3 \int_{\Gamma_e} t_{jk}^e u_{ij}^* \Psi_k(\mathbf{y}) d\Gamma(\mathbf{y}) - \sum_{e=1}^{ne} \sum_{k=1}^3 \int_{\Gamma_e} u_{jk}^e t_{ij}^* \Psi_k(\mathbf{y}) d\Gamma(\mathbf{y}) \quad (7)$$

where  $ne$  is the total number of boundary elements used in the discretization.

In the current application where the domain consists of zoned-homogeneous regions representing the fibers and the matrix material, a boundary integral equation is written for each region. Collocating Eq. 7 at the boundary element nodes yields a system of linear equations relating the components of traction to the components of displacement. These equations can be represented symbolically as

$$[H^i] \{\mathbf{u}^i\} = [G^i] \{\mathbf{t}^i\}, \quad i = 1, N+1 \quad (8)$$

where  $N$  is the number of inclusions, the superscript  $i$  represents the region number, and  $\{\mathbf{u}^i\}$  and  $\{\mathbf{t}^i\}$  represent the components of displacement and traction, respectively, at the collocation nodes. The entries in the matrices  $[H^i]$  and  $[G^i]$  are determined by assembling the numerical values for the integrals on the right-hand side of equation 7.

On the outer boundary of the matrix material, either the displacement or the traction is prescribed. On the interfacial nodes between fiber and matrix, neither the displacement nor traction components are known *a priori*. The system of equations is closed by setting the following interfacial boundary conditions.

$$\{u_j^i\} - \{u_j^m\} = [u] \quad (9)$$

$$\{t_j^i\} = -\{t_j^m\} \quad (10)$$

where  $[u]$  represents a jump in displacement along the interface as discussed in the next section, the superscript  $i$  and  $m$  represent the zoned-homogeneous region, and the subscript represents the global node.

### 3. THE DECOHESION MODEL

Initially, all interfaces between the matrix material and the inclusions are assumed to be perfectly bonded, that is, continuity of traction and displacement is assumed along the interface. The composite is then incrementally stressed by assuming displacements along the outer boundary of the matrix material. At each increment of displacement, the boundary integral equations are solved and the tractions along all interfaces are evaluated. The development of damage (decohesion) is determined through the use of a damage function  $F$  given by

$$F = \left[ \left( \frac{\tau_n}{\tau_{nf}} \right)^2 + \left( \frac{\tau_t}{\tau_{tf}} \right)^2 \right]^{\frac{1}{2}} - f \quad \text{when } \tau_n \geq 0$$

$$F = \left| \frac{\tau_t}{\tau_{tf}} \right| - f \quad \text{when } \tau_n < 0 \quad (11)$$

where  $\tau_n$  is the normal component of traction,  $\tau_t$  is the tangential component of traction,  $\tau_{nf}$  is the value of failure initiation traction in a pure tensile mode,  $\tau_{tf}$  is the value of failure initiation traction in a pure shear mode, and  $f$  is the so-called softening function. The function  $F$  is defined so that no damage occurs if  $F < 0$  and  $F > 0$  is not allowed. Damage develops only if  $F = 0$ . The softening function  $f$  is chosen so that  $f = 1$  for an undamaged interface and  $f = 0$  for a fully decohered interface. For  $0 < f < 1$ , a linear relationship is chosen between the absolute value of the jump in displacement  $[\mathbf{u}]$  at the interface so  $f$  is given by

$$f = 1 - \frac{|[\mathbf{u}]|}{u_0} \quad (12)$$

where the model parameter  $u_0$  is the value of  $|\mathbf{u}|$  at which complete decohesion has occurred. Although the choice of  $f$  is somewhat arbitrary, in the special case of uniaxial tension, the softening function translates into a curve of normal traction versus normal displacement discontinuity in which case the area under the curve is the fracture energy,  $G_f$  defined by

$$G_f = \frac{1}{2} \tau_{nf} u_0 \quad (13)$$

where here  $u_0$  is interpreted as the magnitude of the jump in normal displacement  $[\mathbf{u}_n]$  at which separation occurs. A similar statement holds for a pure mode II (shear) response, and a general statement can be made for mixed mode failure. Note that Eq. 11 could equally well be replaced with a Coulomb model, especially if  $f = 0$ , if such a model is considered to be more representative of physical behavior at debonded interfaces.

After each increment of displacement, the damage function  $F$  is evaluated at each interfacial node. If  $F > 0$ , the threshold to initiate decohesion has been exceeded and is not allowed by the decohesion model. As an example, if the traction at an interfacial node had no tangential component,  $F > 0$  would imply that  $\tau_{nf}$  had been exceeded. In order to drive  $F$  to within a specified tolerance  $\epsilon$  of 0, the following algorithm is used. First, the node is identified at which the largest positive value of  $F$  has been calculated. Next, a jump in displacement at that node is determined by the following evolution equation

$$\Delta [\mathbf{u}] = \Delta \lambda \mathbf{g} \quad (14)$$

where  $[\mathbf{u}] = \left\{ [\mathbf{u}]_n^2 + [\mathbf{u}]_t^2 \right\}^{\frac{1}{2}}$ ,  $\mathbf{g} = \frac{\partial F}{\partial \mathbf{r}}$ , and  $\Delta \lambda = \delta \lambda_1 + \delta \lambda_2 + \dots$

The secant algorithm is applied to determine  $\Delta \lambda$  in order to bring  $F$  to within a tolerance  $\epsilon$  of 0. An initial small value for  $\delta \lambda_1$  is assumed. This then provides the initial assumed value for  $\Delta [\mathbf{u}]$  as shown in Eq. 14. This jump in displacement provides stress relief which is quantified by performing the boundary element analysis with the modified boundary conditions (Eq. 9). The damage function is re-evaluated at the node. If  $F$  is still positive and above the tolerance,  $\delta \lambda_2$  is determined using the equation

$$\delta \lambda_2 = \delta \lambda_1 \frac{F_1}{F_0 - F_1} \quad (15)$$

where the subscript on  $F$  indicates the iteration number. The procedure is continued until  $F < \epsilon$ . In the majority of cases, 2 to 3 iterations were used in the secant method to drive  $F$  below the tolerance. The maximum number of iterations required was 8. During any iteration, if  $[[\mathbf{u}]]$  reaches  $u_0$ , the boundary condition at that node is set to traction free indicating that the node is completely decohered.

Once the damage function  $F$  is reduced below the tolerance or the node becomes completely decohered, a search is performed for the next highest positive value of  $F$  at the remaining nodes, and the process is repeated to reduce  $F$  at that node to below the tolerance. Once the damage function at all nodes is below the tolerance, the next increment in displacement is applied.

#### 4. RESULTS

The composite material considered in this research is composed of an aluminum matrix with embedded boron fibers, which is widely used because of its light weight and versatility. The phase properties are  $E_{al} = 67.51GPa$ ,  $\nu_{al} = 0.35557$ ;  $E_{boron} = 413.04GPa$ ,  $\nu_{boron} = 0.2$ . The two geometries shown in Fig. 1 are investigated. For each geometric configuration, the total areal fraction of the fiber(s) is 20%. Both tensile and shear tests are performed. Two additional configurations with embedded fibers were also considered, namely, two horizontally-alligned

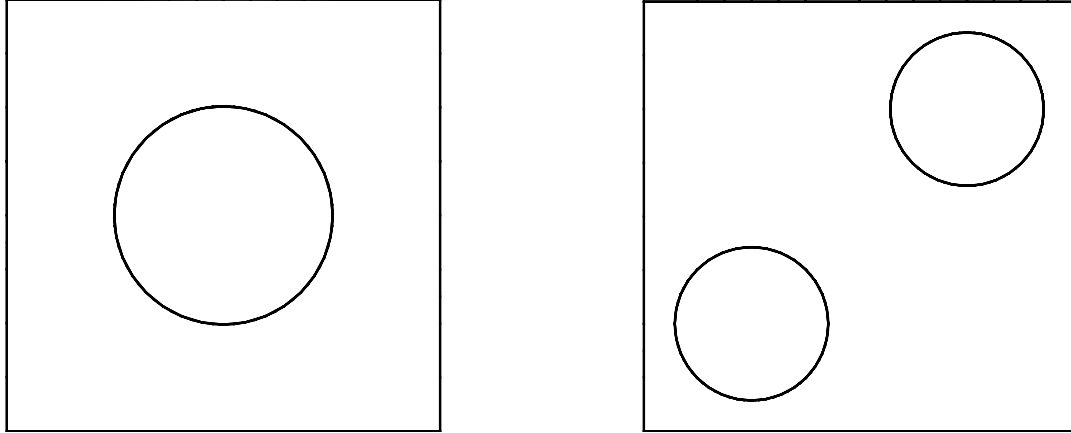


Figure 1. The geometry of one and two boron fiber inclusion(s) in an aluminum matrix at areal fraction of 20%.

fibers and two vertically-aligned fibers. However, the results were similar to the two cases shown in Figure 1 and are not included here.

In the tensile tests, an incremental uniform tensile displacement loading is applied to the left and right lateral sides of the square domain while the top and bottom sides are traction free. In the shear tests, the right lateral side of the domain is subjected to uniform upward shear displacement loading, the left lateral side is subjected to a uniform downward shear displacement loading, and the top and bottom sides are again traction free. In both the tensile and shear tests, the increment of displacement is  $0.0005a$  where  $a$  is the length of the sides of the square specimen. Appropriate boundary constraints are imposed in the boundary element formulation to remove the rigid body modes and maintain a well-posed problem.

For all tests considered, the normal failure parameter is chosen as  $\tau_{nf} = 1.2$ . Two values are chosen for the shear failure parameter, namely,  $\tau_{tf} = 0.6$  and  $\tau_{tf} = 6.0$ . Hence, in one case,  $\tau_{tf}/\tau_{nf} = 0.5$  and, in the other case,  $\tau_{tf}/\tau_{nf} = 5.0$ . Roughly speaking, as the shear failure parameter is increased, the dominant failure mode transitions from shear to normal, or equivalently, from ductile to brittle failure. The value in jump displacement at which complete decohesion is assumed to have occurred is chosen as  $u_0 = 0.01$ .

A series of convergence tests were run to insure the adequacy of the mesh density. As an example for the single inclusion geometry, results were obtained for the tensile test using a coarse mesh containing 68 nodes on the outer boundary of the matrix material and 64 nodes on the interface between the inclusion and matrix material and using a fine mesh containing 164 nodes on the outer boundary and 128 nodes on the interface. Before the onset of decohesion, relative errors between components of traction and displacement making up the solution vector were on the order of  $10^{-6}$ . (Note that all computations were performed in double precision.) Because of the discrete nature of the decohesion algorithm, a true convergence test after the

onset of decohesion is problematic. However, the relative error between the integrated normal traction on the right outer edge of the specimen between the two meshes was less than 3.8% during the entire incremental procedure, and during most incremental steps was less than 1%. This integrated normal traction is a relevant parameter to consider since, as discussed later, it is used to determine the effective Young's modulus. The actual plot of the normalized effective Young's modulus using the coarse and fine meshes is shown at the end of this section. Based on the convergence tests, the coarse mesh was used in the subsequent results.

The first case considered is the single inclusion undergoing a tensile test. The progression of failure for the two values of the shear failure parameter,  $\tau_{tf}$ , are shown in Figs. 2 and 3. The arrows indicate the displacement jump along the interface between the matrix and inclusion, and are magnified by a factor of 10. Although the geometry and loading are symmetric, symmetry is lost as soon as the failure model is first implemented since any jump in displacement is implemented only one node at a time as described in the previous section.

For the first case where  $\tau_{tf} = 0.5\tau_{nf}$ , the decohesion process starts at the leftmost node (Fig. 2(a)). Since the dominant failure mode in this case is the shear mode, the failure progresses predominantly along the left side of the inclusion towards the top and bottom of the inclusion in the tangential (shear) directions (Fig. 2(b)). Near the top and bottom of the inclusion, the stresses are compressive (normal) and the failure abates along the left side of the inclusion as the debonding region approaches these compressive regions. Upon further loading, decohesion progresses along the right side of the inclusion towards the compressive regions on the top and bottom of the inclusion (Figs. 2(c,d)).

For the second case where  $\tau_{tf} = 5.0\tau_{nf}$ , the debonding process again starts at the leftmost node. However, in this case since the shear (sliding) mode of failure is inhibited, the debonding process is seen to occur far more symmetrically (Fig. 3). The failure progresses along both sides of the inclusion almost simultaneously moving towards the top and bottom of the inclusion until the compressive zones are reached.

The second case considered is a single inclusion undergoing a shear test. Results for the two different values of  $\tau_{tf}$  are shown in Figs. 4 and 5. For the case  $\tau_{tf} = 0.5\tau_{nf}$  (Fig. 4), the debonding process starts along the interface at an angle of  $45^\circ$  from the center of the inclusion and progresses towards the compressive regions in the second and fourth quadrants. When the failure region reaches the compressive region, a new failure zone is initiated in the third quadrant originating at an angle of  $225^\circ$ . This new failure region again progresses until reaching the compressive zones in the second and fourth quadrants. For the case  $\tau_{tf} = 5\tau_{nf}$  (Fig. 5), the failure pattern is seen to be far more symmetric about the line of symmetry angled at  $135^\circ$  from horizontal similar to the symmetry seen in the tensile test. The failure progresses from the initiation points at  $45^\circ$  and  $225^\circ$  towards the compressive zones more or less simultaneously on both sides of the inclusion.

Effective elastic constants have been defined for a variety of composite materials containing a dispersed phase ([25, 14, 21]). For the tensile case, an effective Young's modulus can be determined by first integrating the normal traction over either lateral side of the specimen to determine the resultant normal force,  $F_n$ . The effective Young's modulus  $E_{eff}$  of the composite is then given by

$$E_{eff} = \frac{F_n}{a \cdot d} \quad (16)$$

where  $a$  is the length of the lateral side over which the normal displacement of  $d/2$  is applied.

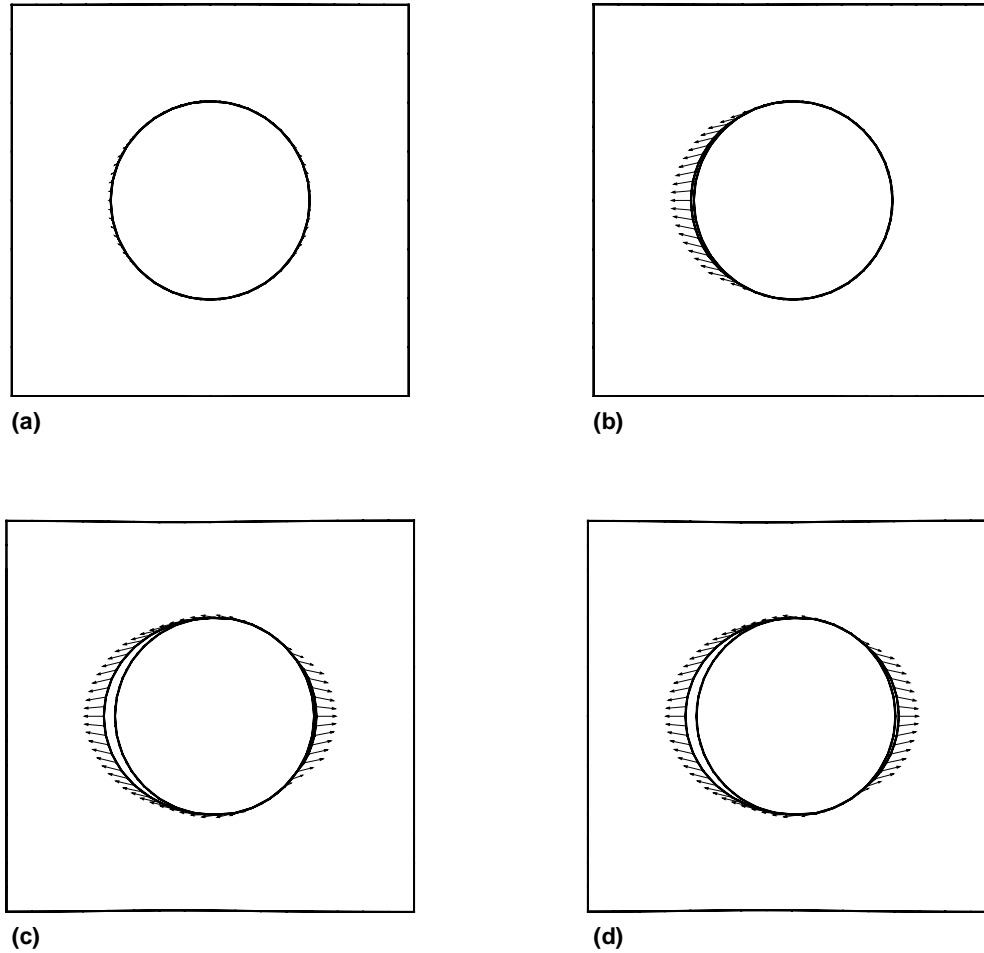


Figure 2. The progression of failure for the tensile test with  $\tau_{tf}/\tau_{nf} = 0.5$ . The normal displacements (nondimensionalized by the length of the side of the specimen) are given by (a) 0.0098, (b) 0.01, (c) 0.037, and (d) 0.039.

The effective Young's modulus can then be normalized as follows

$$E_{nor} = \frac{E_{eff}}{E_{mat}} \quad (17)$$

where  $E_{mat}$  is the Young's modulus of the matrix material.

The normalized Young's modulus as a function of the imposed lateral normal displacement for the two values of  $\tau_{tf}$  is shown in Fig. 6. For the case of  $\tau_{tf} = 0.5\tau_{nf}$ , there are essentially three plateau regions for the normalized effective Young's modulus. The first plateau occurs for small displacements where  $E_{nor} \approx 1.27$  indicating the increase in the Young's modulus

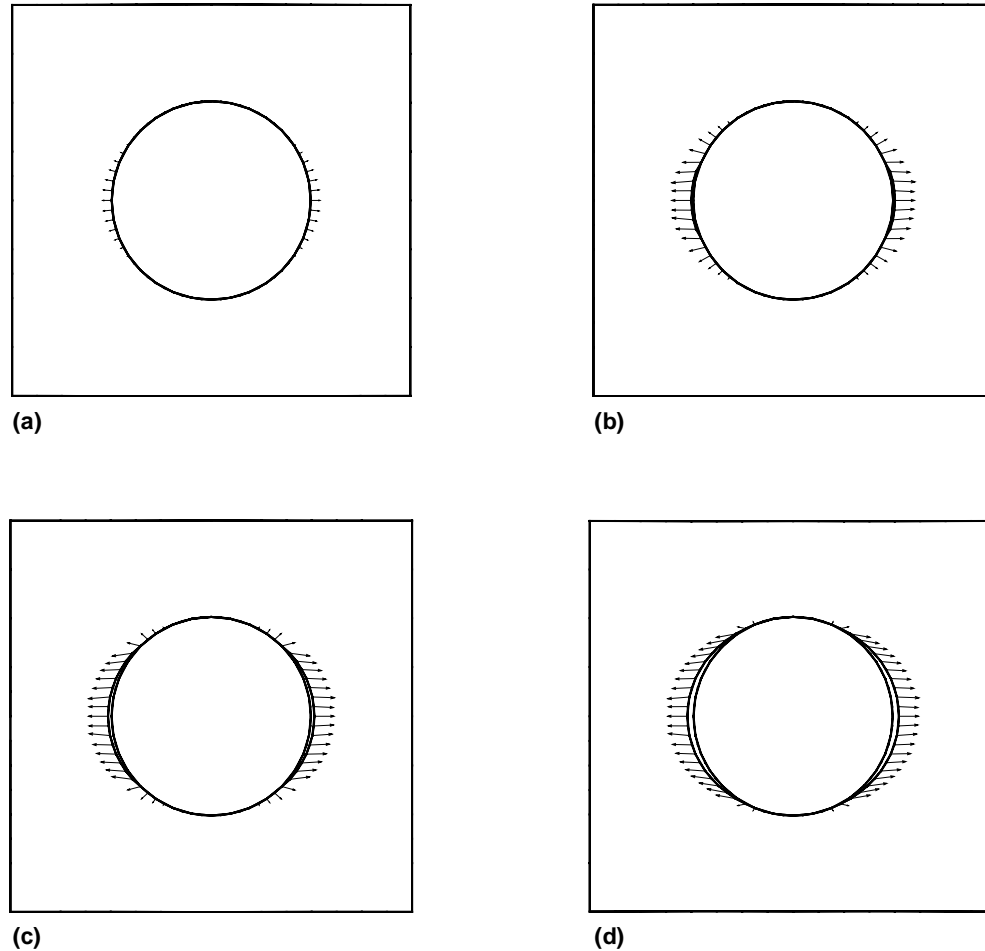


Figure 3. The progression of failure for the tensile test with  $\tau_{if}/\tau_{nf} = 5.0$ . The normal displacements (nondimensionalized by the length of the side of the specimen) are given by (a) 0.013, (b) 0.016, (c) 0.022, and (d) 0.35.

caused by the boron reinforcement. The second plateau is a little less distinct and occurs at  $E_{nor} \approx 0.65$  which corresponds to the decohesion region along the left side of inclusion before the onset of decohesion along the right hand side of the inclusion. The third plateau occurs at  $E_{nor} \approx 0.56$  and corresponds to decohesion along both sides of the inclusion. There is a precipitous drop off from the first plateau to the second plateau corresponding to decohesion progressing along the left hand side of the inclusion. There is a less severe drop off from the second plateau to the third plateau corresponding to the decohesion progressing along the right side of the inclusion.

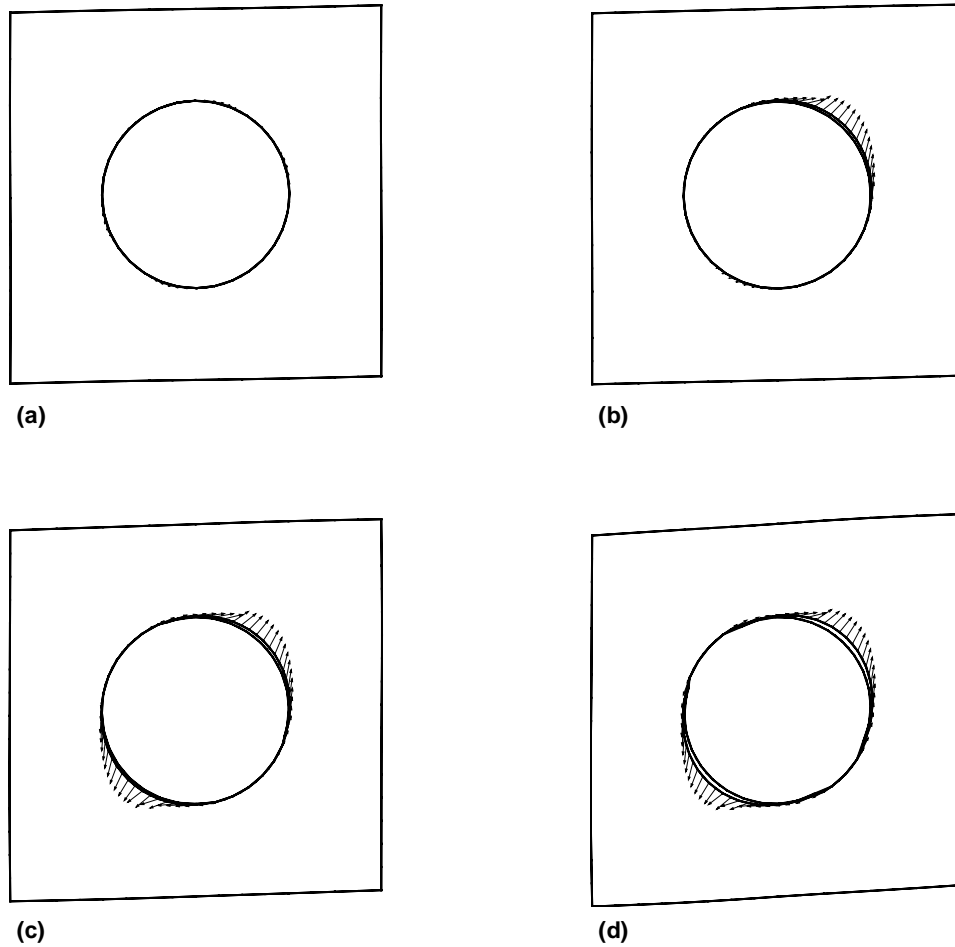


Figure 4. The progression of failure for the shear test with  $\tau_{tf}/\tau_{nf} = 0.5$ . The tangential displacements (nondimensionalized by the length of the side of the specimen) are given by (a) 0.02, (b) 0.0235, (c) 0.03, and (d) 0.58.

For the case of  $\tau_{tf} = 5.0\tau_{nf}$ , there are essentially only two plateaus at  $E_{nor} \approx 1.28$  and  $E_{nor} \approx 0.68$  corresponding to the initially undamaged material and the completely decohered interface in the tensile regions, respectively. There is a far smoother transition between the plateaus as compared to the case where  $\tau_{tf} = 0.5\tau_{nf}$ . This is a result of the fact that the decohesion process occurs far more symmetrically.

In a similar manner, an effective shear modulus can be determined for the shear test by integrating the shear traction over either lateral side of the specimen to determine the resultant

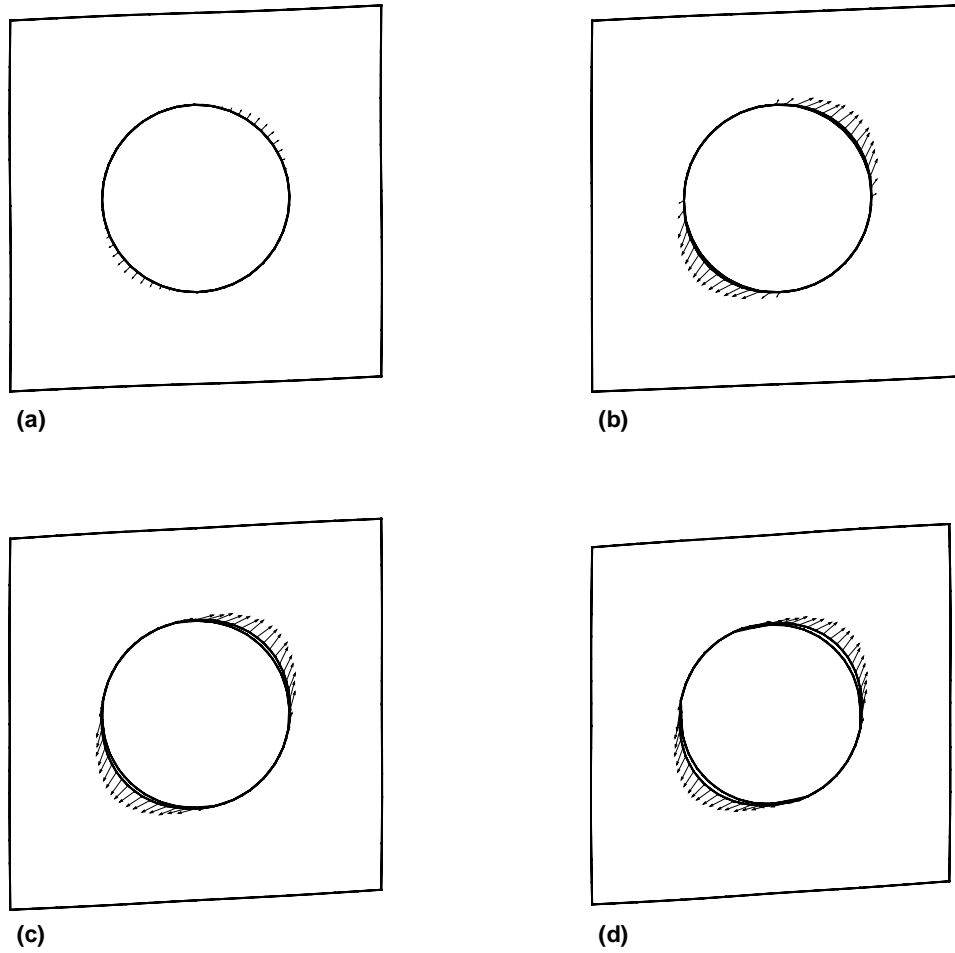


Figure 5. The progression of failure for the shear test with  $\tau_{tf}/\tau_{nf} = 5.0$ . The tangential displacements (nondimensionalized by the length of the side of the specimen) are given by (a) 0.041, (b) 0.042, (c) 0.054, and (d) 0.65.

shear force,  $F_s$ . The effective shear modulus  $G_{eff}$  of the composite is then given by

$$G_{eff} = \frac{F_s}{a \cdot d} \quad (18)$$

where, in this case, a tangential displacement of  $d/2$  is applied. The effective shear modulus can be normalized as follows

$$G_{nor} = \frac{G_{eff}}{G_{mat}} \quad (19)$$

where  $G_{mat}$  is the shear modulus of the matrix material.

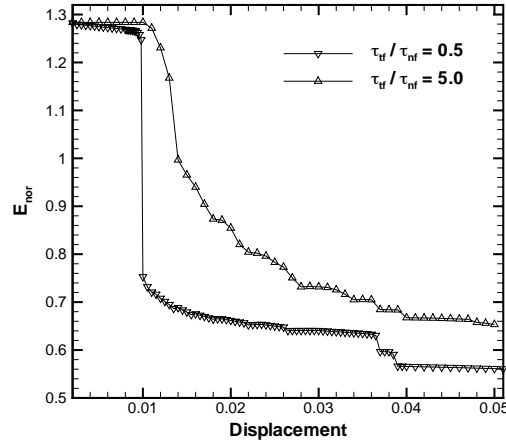


Figure 6. The normalized effective Young's modulus as a function of displacement for the single inclusion case undergoing a tensile test.

The normalized shear modulus as a function of the imposed lateral shear displacement for the two values of  $\tau_{tf}$  is shown in Fig. 7. For the case of  $\tau_{tf} = 0.5\tau_{nf}$ , the three plateaus are even more distinct than seen in the corresponding tensile test (Fig. 6). These plateaus, occurring at  $G_{nor} \approx 1.31$ ,  $G_{nor} \approx 1.00$ , and  $G_{nor} \approx 0.88$ , correspond to no decohesion, decohesion in the first quadrant only, and decohesion in the first and third quadrant, respectively. For the case of  $\tau_{tf} = 5.0\tau_{nf}$ , there are essentially only two plateaus at  $G_{nor} \approx 1.32$  and  $G_{nor} \approx 0.98$  corresponding to the initially undamaged material and the completely decohered interface in the first and third quadrants. The second plateau is again eliminated in this case since the decohesion progresses almost simultaneously in the first and third quadrants. Similar to the tensile test, the augmentation of the shear modulus of the composite specimen due to the boron inclusion deteriorates rapidly as the decohesion process progresses.

The next geometry considered is two inclusions with their line-of-centers making a  $45^\circ$  angle with the horizontal. The results for the progression of failure in the tensile test is shown in Fig. 8 for the case  $\tau_{tf}/\tau_{nf} = 0.5$  and in Fig. 9 for the case  $\tau_{tf}/\tau_{nf} = 5.0$ . For the case  $\tau_{tf}/\tau_{nf} = 0.5$ , the decohesion is seen to progress first along the outer sides of the two inclusions, that is, the two sides nearest the edges of the composite specimen. Once these decohered outer portions of the interface reach the compressive regions on the top and bottom of the inclusions, the inner portions of the interfaces begin to decohere. Similar to the case of one inclusion when the shear failure mode is dominant, the decohered damaged portion of the interface slides along one side of each inclusion before the decohesion process begins along the other side of the inclusion. For the case in which  $\tau_{tf}/\tau_{nf} = 5.0$ , the decohesion progresses fairly simultaneously along both sides of both inclusions from the tensile to the compressive regions along the interface since the shear failure mode is inhibited as seen in Fig. 9. Unlike the single inclusion case, the displacement jump is seen to be somewhat larger along the outer sides of the two inclusions which is caused by the fact that the outer edge is far closer to the edge of the specimen where the normal displacement is imposed.

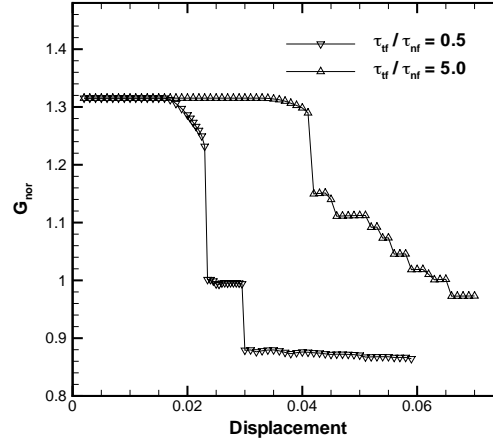


Figure 7. The normalized effective shear modulus as a function of displacement for the single inclusion case undergoing a shear test.

For the shear test, the results for the progression of failure are shown in Fig. 10 for the case  $\tau_{tf}/\tau_{nf} = 0.5$  and in Fig. 11 for the case  $\tau_{tf}/\tau_{nf} = 5.0$ . As seen in Fig. 10 for the mode dominated by shear failure, the decohesion progresses one side at a time. That is, the decohesion starts in the third quadrant of the upper right inclusion and progresses towards the compressive zones in the second and fourth quadrants, then sequentially continues in the first quadrant of the lower left inclusion, the third quadrant of the lower left inclusion, and finally, the first quadrant of the upper right inclusion. Once decohesion begins along a side, the sliding failure takes over and decohesion continues exclusively along that side until the compressive zones are reached. By contrast as seen in Fig. 11 for the mode dominated by normal failure, the decohesion begins fairly simultaneously in the third quadrant of the upper right inclusion and the first quadrant of the lower left inclusion, and subsequently, simultaneously in the first quadrant of the upper right inclusion and the third quadrant of the lower left inclusion.

The normalized Young's modulus as a function of the imposed lateral normal displacement for the two values of  $\tau_{tf}$  is shown in Fig. 12. Similar to the single inclusion specimen, for the case  $\tau_{tf} = 0.5\tau_{nf}$ , there are essentially three plateau regions for the normalized effective Young's modulus. The first plateau region at small displacements where  $E_{nor} \approx 1.26$  results from the increase in the Young's modulus caused by the two boron reinforcements. The second plateau region at  $E_{nor} \approx 0.6$  is less distinct and corresponds to the decohesion region along the outside of the two inclusions but before the onset of decohesion along the inside of the two inclusions. The third plateau occurs at  $E_{nor} \approx 0.5$  and corresponds to decohesion along all four sides of the two inclusions.

The normalized shear modulus as a function of the imposed shear displacement for the two values of  $\tau_{tf}$  is shown in Fig. 13. For the case  $\tau_{tf} = 0.5\tau_{nf}$ , there are four distinct plateaus of the normalized shear modulus at  $G_{nor} \approx 1.35$ ,  $G_{nor} \approx 1.15$ ,  $G_{nor} \approx 1.1$ , and  $G_{nor} \approx 0.9$ . The plateaus can be identified as corresponding to the undamaged material, decohesion in the third quadrant of the upper right inclusion, decohesion in the third quadrant of the upper

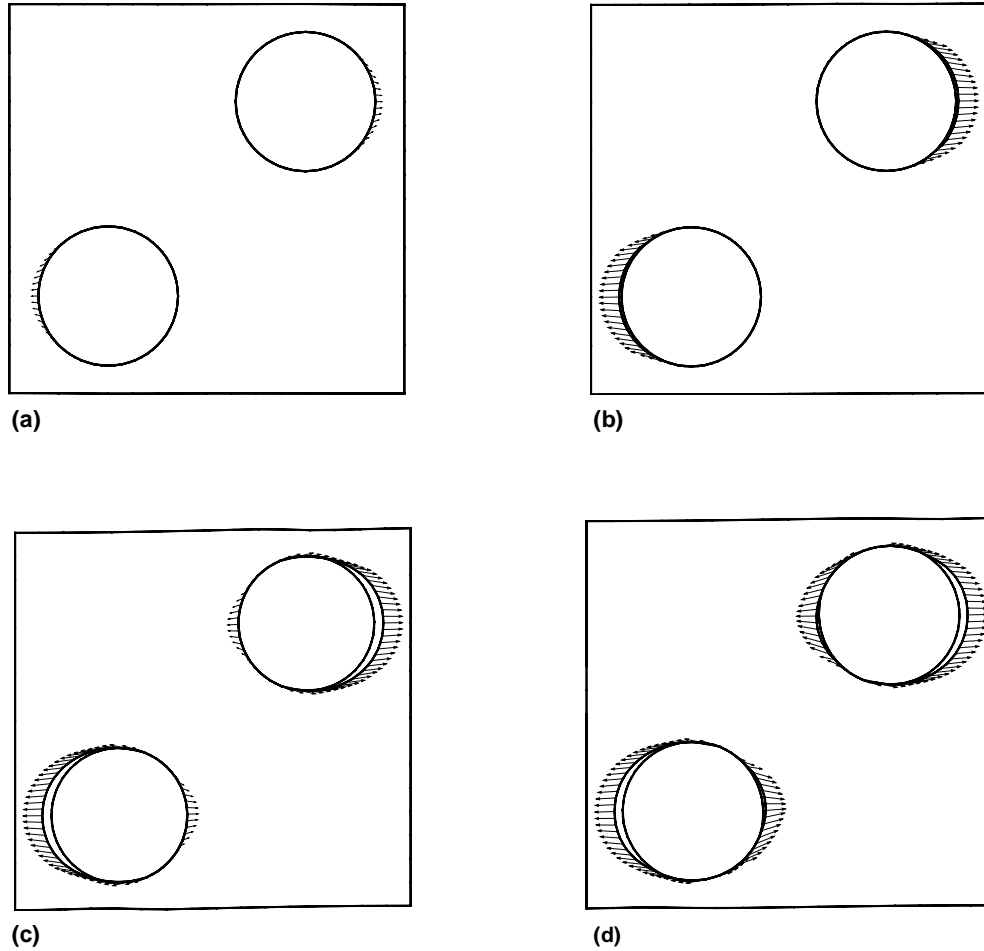


Figure 8. The progression of failure for the tensile test with  $\tau_{tf}/\tau_{nf} = 0.5$ . The normal displacements (nondimensionalized by the length of the side of the specimen) are given by (a) 0.011, (b) 0.012, (c) 0.04, and (d) 0.045.

right inclusion and the first quadrant of the lower left inclusion, and decohesion in the first and third quadrants of both inclusions, respectively. However, there appears to be a missing plateau corresponding to decohesion in the first and third quadrants of the lower left inclusion and in the third quadrant of the upper right inclusion as seen in Fig. 10(c). It is possible that this missing plateau might only occur over a very small range of shear displacements and is not seen in Fig. 13 because the increment of shear displacement was too large. For the case  $\tau_{tf} = 5.0\tau_{nf}$ , the relationship between shear displacement and the normalized shear modulus is more irregular resulting from the way in which the decohesion model is implemented. That

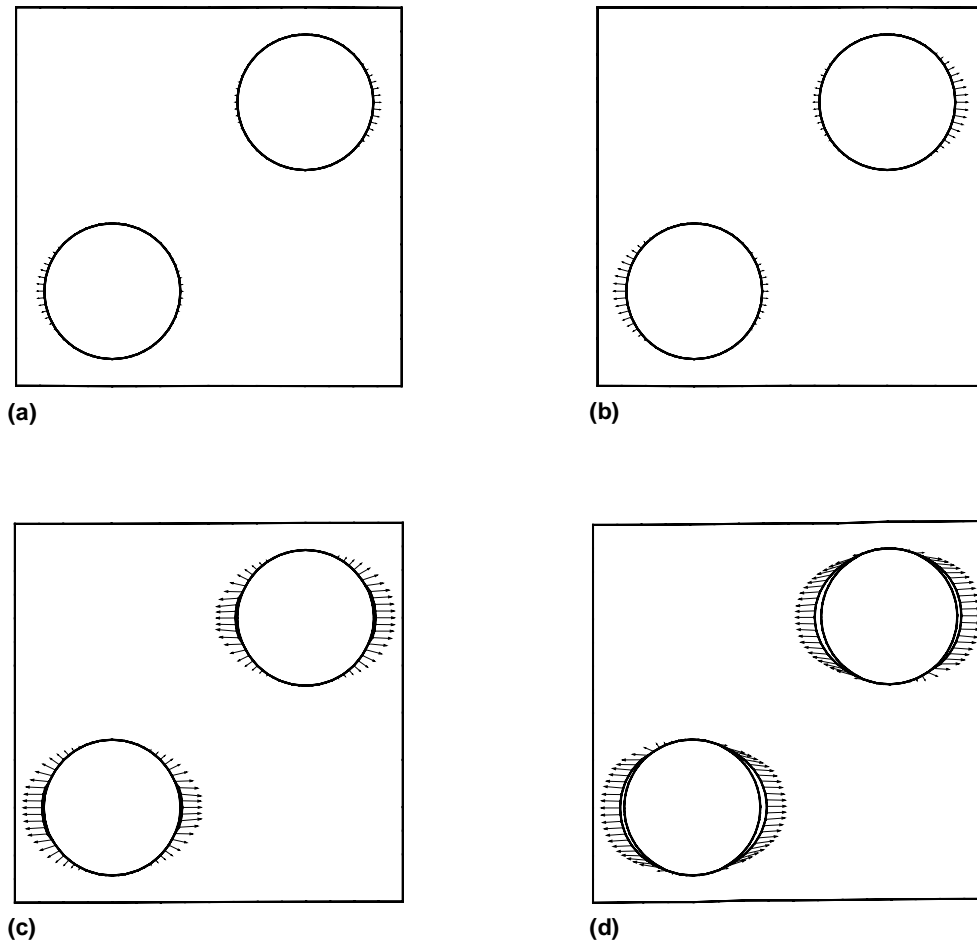


Figure 9. The progression of failure for the tensile test with  $\tau_{if}/\tau_{nf} = 5.0$ . The normal displacements (nondimensionalized by the length of the side of the specimen) are given by (a) 0.014, (b) 0.016, (c) 0.02, and (d) 0.04.

is, the displacement jumps are imposed one node at a time depending on where the maximum of the damage function exists.

Finally, as discussed at the beginning of this section, a comparison of the numerical results for the normalized Young's modulus is shown in Fig. 14 using the coarse and fine meshes. The specific case considered is for the single inclusion geometry and  $\tau_{if}/\tau_{nf} = 5.0$ . Again, the coarse mesh contained 68 nodes on the outer boundary of the matrix material and 64 nodes on the interface between the inclusion and matrix material and the fine mesh contained 164 nodes on the outer boundary and 128 nodes on the interface. As seen in the figure, the two curves

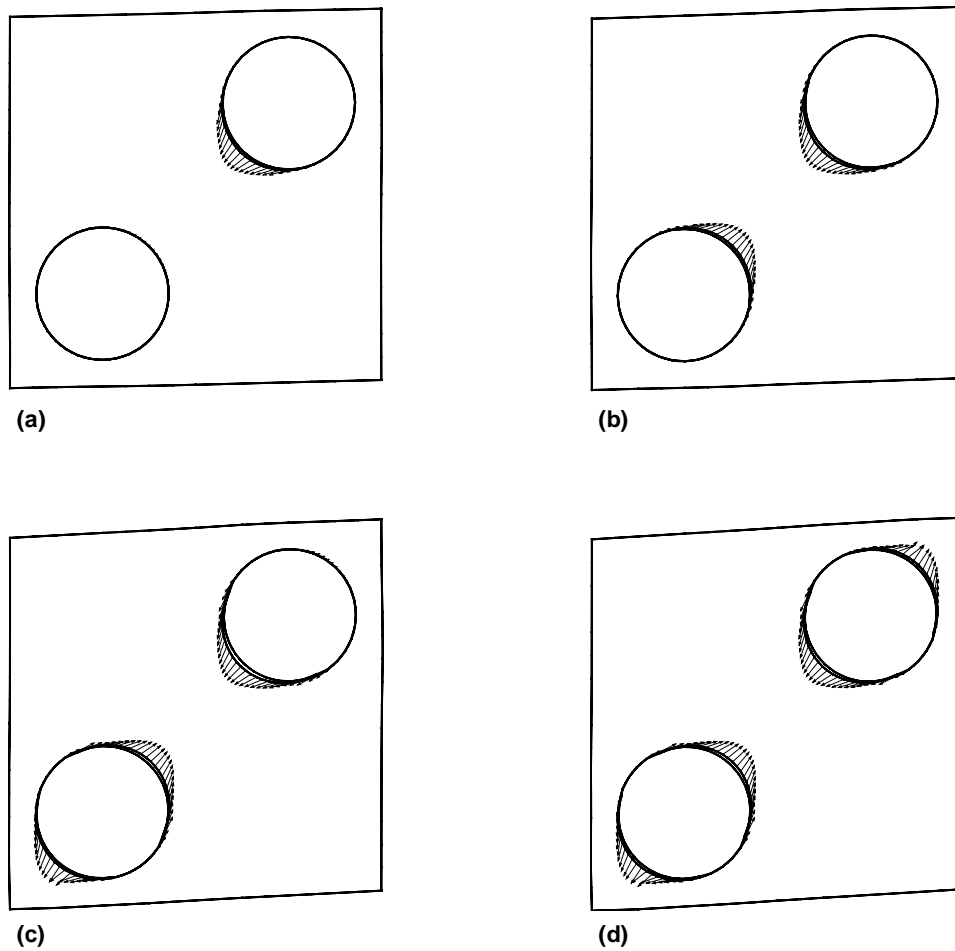


Figure 10. The progression of failure for the shear test with  $\tau_{tf}/\tau_{nf} = 0.5$ . The tangential displacements (nondimensionalized by the length of the side of the specimen) are given by (a) 0.022, (b) 0.032, (c) 0.05, and (d) 0.58.

follow each other closely with the largest relative discrepancy being approximately 3.8%. This shows that the solution using the coarse mesh has achieved an acceptable level of convergence especially in light of the discrete nature of the decohesion algorithm.

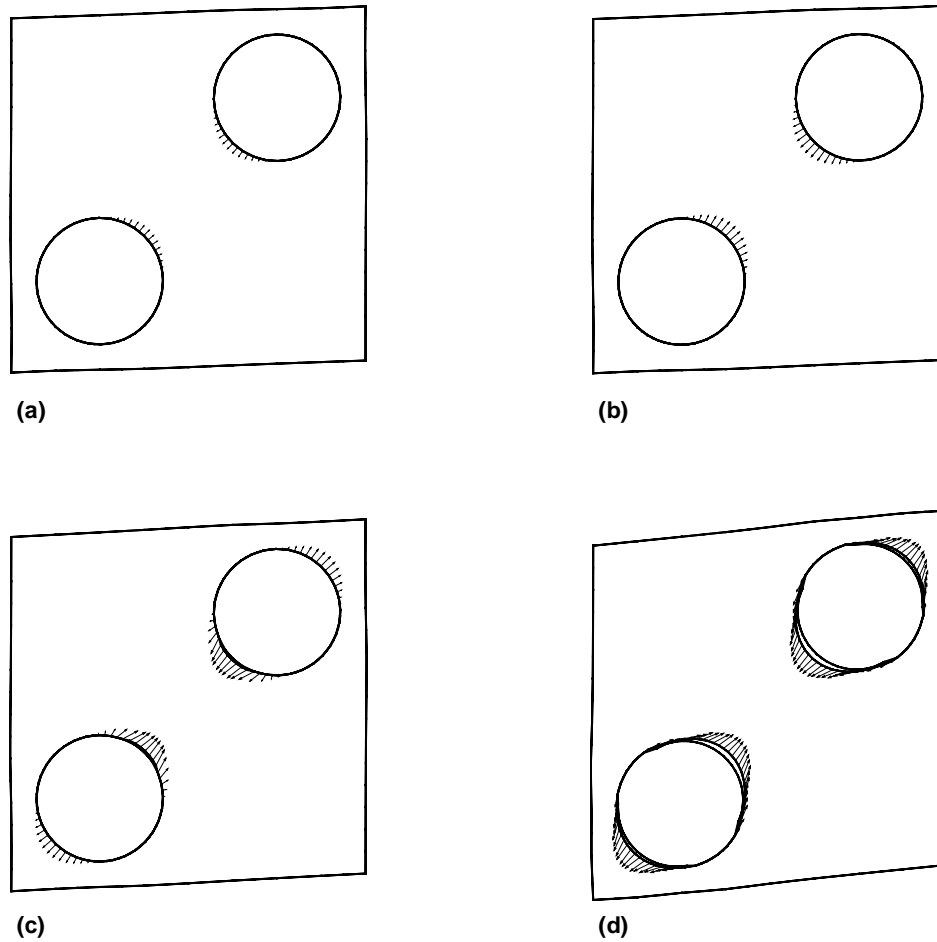


Figure 11. The progression of failure for the shear test with  $\tau_{tf}/\tau_{nf} = 5.0$ . The tangential displacements (nondimensionalized by the length of the side of the specimen) are given by (a) 0.034, (b) 0.038, (c) 0.05, and (d) 0.99.

## 5. CONCLUSIONS

A softening decohesion model has been combined with linear elasticity to describe the evolution of interfacial failure in fiber-reinforced materials. As softening occurs, the sum of the work performed by the traction and the stored energy released by the material equals the energy dissipated. Progressive evolution of the debonding zones and the propagation of decohesion along the interface have been illustrated by incremental simulations. The material failure parameters,  $\tau_{nf}$  and  $\tau_{tf}$ , play an important role in the decohesion process and may explain

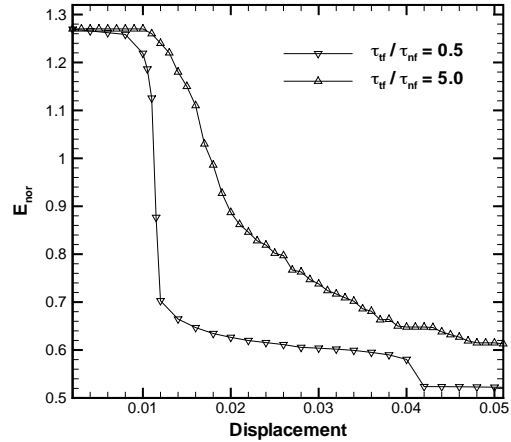


Figure 12. The normalized effective Young's modulus as a function of displacement for the two inclusion case undergoing a tensile test.

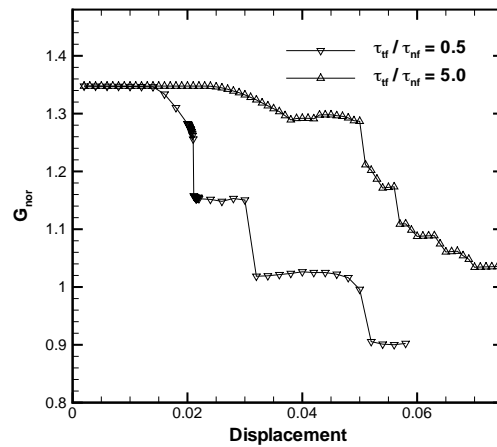


Figure 13. The normalized effective shear modulus as a function of displacement for the two inclusion case undergoing a shear test.

the difference between failure in ductile and brittle materials. In particular, if the ratio  $\tau_{tf}/\tau_{nf}$  is small, then the material is more likely to fail in shear. In these cases once a portion of the interface becomes partially decohered, the damage zone slides tangentially along the interface until a compressive region is reached. On the other hand, if  $\tau_{tf}/\tau_{nf}$  is large, then this shear mode failure is inhibited and damage tends to progress simultaneously on both sides of the inclusion. Decohesion has significant effect on the macroscopic response of the composite

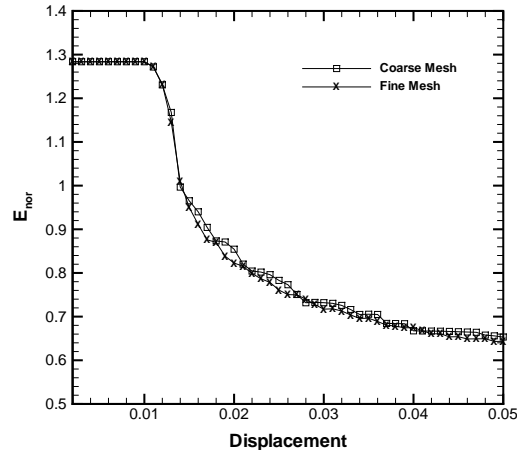


Figure 14. The normalized effective Young's modulus as a function of displacement for calculations using the coarse and fine meshes.

materials. In particular, the effective composite properties are adversely affected to the point where the partially decohered inclusion can actually diminish the effective shear and Young's moduli.

## 6. BIBLIOGRAPHY

### REFERENCES

1. J. S. Agaipou. An experimental determination of the thermal conductivity of a 304L stainless steel powder metallurgy material. *J. Heat Trans.*, 111:281–286, 1989.
2. M. Avellaneda and G. W. Milton. Optimal bounds on the effective bulk modulus of polycrystals. *SIAM J. Appl. Math.*, 49:824–837, 1989.
3. C. A. Brebbia, J. C. F. Telles, and L. C. Wrobel. *Boundary Element Techniques. Theory and Applications in Engineering*. Springer-Verlag, Berlin, 1984.
4. M. K. Chati and A. K. Mitra. Prediction of elastic properties of fiber-reinforced unidirectional composites. *Eng. Anal. Bound. Elem.*, 21(3):235–244, 1998.
5. H. Cheng and S. Torquato. Effective conductivity of periodic arrays of spheres with interfacial resistance. *Proc. R. Soc. Lond. A.*, 453:145–161, 1997.
6. T.-W. Chou, S. Nomura, and M. Taya. A self-consistent approach to the elastic stiffness of short-fiber composites. *J. Comp. Mat.*, 14:178–188, 1980.
7. M. E. Cruz and A. T. Patera. A parallel Monte-Carlo finite element procedure for the analysis of multicomponent random media. *Int. J. Num. Meths. Engrg.*, 38(7):1087–1121, 1995.
8. L. C. Davis. Third order bounds on the elastic moduli of metal matrix composites. *Metal. Trans.*, 22A:3065–3067, 1991.
9. Z. Hashin. Analysis of composite materials: A survey. *J. Appl. Mech.*, 50:481–505, 1983.
10. Z. Hashin. Thermoelastic properties of particulate composites with imperfect interface. *J. Mech. Phys. Solids*, 39(6):745–762, 1991.

11. Z. Hashin and S. Strikman. A variational approach to the theory of the elastic behavior of multiphase materials. *J. Mech. Phys. Solids*, 11:127–140, 1963.
12. M. S. Ingber, D. E. Womble, and L. A. Mondy. A parallel boundary element formulation for determining effective properties of heterogeneous media. *Int. J. Num. Meths. Engrg.*, 37(22):3905–3920, 1994.
13. E. Juhlin, X. Chen, and T. D. Papathanasiou. On the effects of fiber length and spatial distribution on the stiffness of short-fiber reinforced composites. *Poly. Poly. Comp.*, 10(3):205–210, 2002.
14. Y. S. Lee, T. J. Batt, and P. K. Liaw. A semi-empirical method to characterize effective elastic moduli of components in binary composite materials. *Int. J. Numer. Meth. Engrg.*, 34:651–684, 2000.
15. R. Lipton. Design of particle reinforced heat conducting composites with interfacial thermal barriers. *J. Comp. Mech.*, 32(14):1322–1331, 1998.
16. J. K. MacKenzie. The elastic constants of a solid containing spherical holes. *Proc. Phys. Soc. B*, 63:2–11, 1949.
17. A. Needleman. A continuum model of void nucleation by inclusion debonding. *J. Appl. Mech.*, 54:525–531, 1987.
18. S. Nemat-Nasser and M. Hori. *Micromechanics: Overall Properties of Heterogeneous Materials*. North-Holland Series in Applied Mathematics and Mechanics, 1993.
19. S. Nemat-Nasser, T. Iwakuma, and M. Hejazi. On composites with periodic structure. *Mech. Mat.*, 1:239–267, 1982.
20. J. P. O’Rourke, M. S. Ingber, and M. W. Weiser. The effective elastic constants of solids containing spherical exclusions. *J. Comp. Mat.*, 31(9):910–934, 1997.
21. T. D. Papathanasiou, M. S. Ingber, and Graham A L L. A. Mondy. The effective elastic modulus of fiber-reinforce composites. *J. Comp. Mat.*, 28(4):288–304, 1994.
22. A. Salvadori. A symmetric boundary integral formulation for cohesive interface problems. *Comp. Mech.*, 32:381–391, 2003.
23. A. S. Sangani and G. Mo. Elastic interactions in particulate composites with perfect as well as imperfect interfaces. *J. Mech. Phys. Solids*, 45(11/12):2001–2031, 1997.
24. H. L. Schreyer, D. L. Sulsky, and S. J. Zhou. Modeling delamination as a strong discontinuity with the material point method. *Comp. Meth. Appl. Mech. Engrg.*, 191:2483–2507, 2002.
25. S. Torquato. Random heterogeneous media: Microstructure and improved bounds on effective properties. *Appl. Mech. Rev.*, vol 44(no 2):pp 37–76, 1991.